A&A 564, A118 (2014)
DOI: 10.1051/0004-6361/201322997

Astronomy & Astrophysics

The inner circumstellar disk of the UX Orionis star V1026 Scorpii⋆,⋆⋆

J. Vural[1], A. Kreplin[1], M. Kishimoto[1], G. Weigelt[1], K.-H. Hofmann[1], S. Kraus[2], D. Schertl[1], M. Dugué[3], G. Duvert[4], S. Lagarde[3], and F. Massi[5]

[1] Max-Planck-Institut für Radioastronomie, Auf dem Hügel 69, 53121 Bonn, Germany
e-mail: jvural@mpifr-bonn.mpg.de
[2] University of Exeter, Astrophysics group, Physics Building, Stocker Road Exeter, EX4 4QL, UK
[3] Laboratoire Lagrange, UMR 7293, Université de Nice Sophia-Antipolis, CNRS, Observatoire de la Côte d'Azur, 06300 Nice, France
[4] UJF-Grenoble 1/CNRS-INSU, Institut de Planétologie et d'Astrophysique de Grenoble (IPAG) UMR 5274, 38041 Grenoble, France
[5] INAF – Osservatorio Astrofisico di Arcetri, Largo E. Fermi, 5, 50125 Firenze, Italy

Received 6 November 2013 / Accepted 20 February 2014

ABSTRACT

Context. The UX Ori type variables (named after the prototype of their class) are intermediate-mass pre-main sequence objects. One of the most likely causes of their variability is the obscuration of the central star by orbiting dust clouds.
Aims. We investigate the structure of the circumstellar environment of the UX Ori star V1026 Sco (HD 142666) and test whether the disk inclination is large enough to explain the UX Ori variability.
Methods. We observed the object in the low-resolution mode of the near-infrared interferometric VLTI/AMBER instrument and derived *H*- and *K*-band visibilities and closure phases. We modeled our AMBER observations, published Keck Interferometer observations, archival MIDI/VLTI visibilities, and the spectral energy distribution using geometric and temperature-gradient models.
Results. Employing a geometric inclined-ring disk model, we find a ring radius of 0.15 ± 0.06 AU in the *H* band and 0.18 ± 0.06 AU in the *K* band. The best-fit temperature-gradient model consists of a star and two concentric, ring-shaped disks. The inner disk has a temperature of 1257^{+133}_{-53} K at the inner rim and extends from 0.19 ± 0.01 AU to 0.23 ± 0.02 AU. The outer disk begins at $1.35^{+0.19}_{-0.20}$ AU and has an inner temperature of 334^{+35}_{-17} K. The derived inclination of $48.6^{+2.9}_{-3.6}$° approximately agrees with the inclination derived with the geometric model (49 ± 5° in the *K* band and 50 ± 11° in the *H* band). The position angle of the fitted geometric and temperature-gradient models are 163 ± 9° (*K* band; 179 ± 17° in the *H* band) and $169.3^{+4.2}_{-6.7}$°, respectively.
Conclusions. The narrow width of the inner ring-shaped model disk and the disk gap might be an indication for a puffed-up inner rim shadowing outer parts of the disk. The intermediate inclination of ∼50° is consistent with models of UX Ori objects where dust clouds in the inclined disk obscure the central star.

Key words. stars: individual: V1026 Sco – stars: pre-main sequence – circumstellar matter – techniques: interferometric – accretion, accretion disks – stars: formation

1. Introduction

The UX Ori (UXOr) phenomenon of Herbig Ae/Be stars (HAeBes) is attributed to obscuration by circumstellar dust in an inclined disk (Grinin et al. 1994; Natta et al. 1997; Grinin et al. 2001; Dullemond et al. 2003) or unsteady accretion (Herbst & Shevchenko 1999). The Herbig Ae star V1026 Sco (HD 142666) has a spectral type of A8Ve (Dominik et al. 2003) and is classified as a UX Ori object (Meeus et al. 1998). The UX Ori variability has been confirmed by Zwintz et al. (2009). Dominik et al. (2003) and van Boekel et al. (2005) report distances of 116 pc and 145 ± 43 pc, respectively. We adopt the Hipparcos-based measurement of 116 pc and the associated parameters for our work. The object V1026 Sco shows large, non-periodic (Lecavelier des Etangs et al. 2005) brightness variations (>1.2 mag) and a pulsational variability on the milli-magnitude level (Zwintz et al. 2009). It reddens with decreasing apparent magnitude (Meeus et al. 1998). These authors suggest that dense dust clouds in an inclined disk cause the stellar reddening. Alecian et al. (2013a) report on the magnetic properties of V1026 Sco (and several other Herbig Ae/Be stars). The object V1026 Sco belongs to the Meeus group IIa (Juhász et al. 2010) and might, therefore, have a self-shadowed disk. The stellar parameters (Dominik et al. 2003) of V1026 Sco are listed in Table 1. By modeling the spectral energy distribution (SED), Dominik et al. (2003) found that the circumstellar disk of V1026 Sco has an inclination of approximately 55°. Monnier et al. (2005) have performed Keck Interferometer (KI) measurements of V1026 Sco and found an inner disk diameter of 2.52 mas (0.29 AU at 116 pc). In a recent publication, Schegerer et al. (2013) have reported mid- and near-infrared (NIR) interferometric observations (archival MIDI/VLTI & IOTA data), and performed radiative transfer modeling of V1026 Sco, and derived a disk structure with a gap from 0.35 AU to 0.80 AU.

In this paper, we analyze the circumstellar environment around V1026 Sco by taking new interferometric NIR

⋆ Based on observations made with ESO telescopes at the La Silla Paranal Observatory under programme IDs 083.D-0224(C), 083.C-0236(A), 087.C-0013(A) and 073.A-9014(A).

⋆⋆ Member of the International Max Planck Research School (IMPRS) for Astronomy and Astrophysics at the Universities of Bonn and Cologne.

Table 1. Adopted stellar parameters of HD 142666.

Parameter	Value
spectral type	A8Ve[a]
age [Myr]	6.0 ± 1.5[b]
distance [pc]	116
$M_*[M_\odot]$	1.8
$L_*[L_\odot]$	11
T_*[K]	8500
$\log(\dot{M}[M_\odot\,\mathrm{yr}^{-1}])$	-6.73 ± 0.26[c]

Notes. The values are taken from Dominik et al. (2003) unless otherwise noted. The error bars are shown where available. Dominik et al. (2003) estimate the uncertainty of the luminosity to be ±50% (due to the HIPPARCOS distance error) and the mass uncertainty to be 5–10%. Other authors find slightly different parameters for the alternative distance of 145 ± 20 pc. For example Alecian et al. (2013a) derived $5.0^{+1.6}_{-1.1}$ Myr, $2.15^{+0.20}_{-0.19}\,M_\odot$, $27.5^{+7.9}_{-7.1}\,L_\odot$, and 7900 ± 200 K. Other references: [(a)] Meeus et al. (1998); [(b)] Folsom et al. (2012); [(c)] Mendigutía et al. (2011).

VLTI/AMBER and archival mid-infrared (MIR) VLTI/MIDI measurements into account. We describe our observations and the data reduction in Sect. 2. The modeling is presented in Sect. 3, and our results are discussed in Sect. 4.

2. Observation and data reduction

We observed V1026 Sco on three different nights with the NIR three-beam VLTI/AMBER instrument (Petrov et al. 2007). The observations were performed in low-resolution mode (spectral resolution $R = 30$). Table 2 lists the observational parameters. The uv coverage of our 2009 and 2011 AMBER observations with the published KI and archival MIDI observations of V1026 Sco used in this study are shown in Fig. 1.

We reduced the AMBER data with *amdlib-3.0.2*[1] (Tatulli et al. 2007; Chelli et al. 2009). To improve the calibrated visibility, we processed only 20% of the frames (object and calibrator) with the best fringe signal-to-noise ratio (Tatulli et al. 2007). In addition, we equalized the histograms of the optical path differences (OPD) of the calibrator and the object data, because different histograms (due to OPD drifts caused, for example, by errors of the OPD model) can lead to visibility errors. Histogram equalization can reduce these visibility errors. This method is described in detail in Kreplin et al. (2012).

We were able to extract H and K band visibilities (cf. Fig. 2). Within the error bars, the obtained closure phase is zero for all nights (Fig. 3), which is consistent with a centro-symmetric brightness distribution.

We also used archival low-resolution data obtained with the MIR two-beam combiner MIDI (Leinert et al. 2003; Schegerer et al. 2013). The data (see Table 2) were reduced using our own IDL codes (see Appendix A of Kishimoto et al. 2011 for details), which utilize a part of the standard software EWS[2] and also implement an average over a relatively large number of frames to determine the group-delay and phase-offset tracks with a good signal-to-noise ratio. This is important when dealing with sub-Jy sources, such as our target here. The MIDI visibilities are shown in Fig. 4 (right).

[1] http://www.jmmc.fr/data_processing_amber.htm
[2] http://www.strw.leidenuniv.nl/~nevec/MIDI/index.html

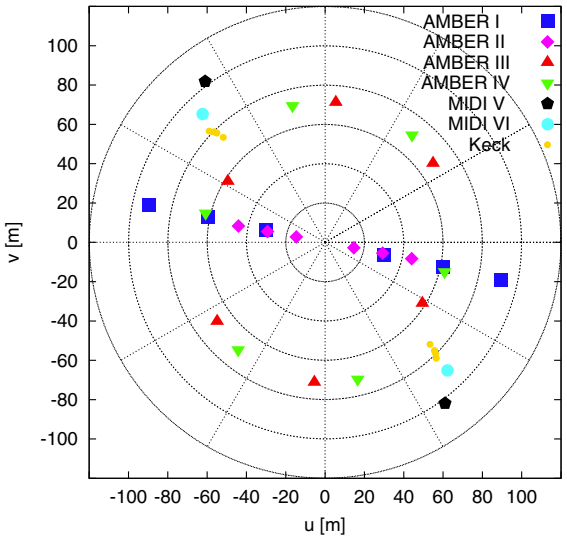

Fig. 1. The uv coverage of all interferometric measurements used (AMBER, MIDI, Keck; see Table 2).

3. Analysis

3.1. Geometric modeling

To estimate the characteristic size of the NIR emission region, we fit geometric models to the visibilities. The model for the NIR data consists of an unresolved stellar contribution and an inclined ring with a width of 20% of its inner radius $r_{\mathrm{ring,in}}$ (which is equal to the semi-major axis in the model). We averaged the different visibility measurements (shown in Fig. 2) of the spectral channels within the H and K bands to obtain wavelength-averaged H- and K-band visibilities (Fig. 5). The resulting visibilities within each band were fit with the model visibilities of the two-dimensional, inclined star-ring model.

In the K band, we included literature data from the Keck interferometer (Monnier et al. 2005, see Fig. 1) in the fit. Because of the almost constant projected baseline length and position angle of the five KI measurements, the data points were averaged.

To fit the visibilities, we derived the NIR flux contribution of the star (f_{star}) from our SED fit (Fig. 6 left) and obtained approximately 0.33 (Monnier et al. 2005 report 0.39) in the K band and 0.53 in the H band. For the total visibility, we obtain

$$|V| = |(1 - f_{\mathrm{star}})V_{\mathrm{disk}} + f_{\mathrm{star}}V_{\mathrm{star}}|\,, \quad (1)$$

where $f_{\mathrm{star}} + f_{\mathrm{disk}} = 1$ and the unresolved star has $V_{\mathrm{star}} = 1$.

We found a semi-major axis ($r_{\mathrm{ring,in}}$) of 1.30 ± 0.14 mas (or 0.15 ± 0.06 AU for a distance of 116 pc) in the H band and 1.57 ± 0.09 mas (or 0.18 ± 0.06 AU) in the K band (Fig. 5). All fitted parameters are listed in Table 3. In the H band, the inclination angle i (angle between the system axis and the viewing direction) is $50 \pm 11°$, and the position angle ϑ of the semi-major axis of the disk is $179 \pm 17°$. In the K band, we derived $i = 49 \pm 5°$ and $\vartheta = 163 \pm 9°$, respectively.

3.2. Temperature-gradient model

To fit all available wavelength-dependent visibilities (AMBER, MIDI, and KI, see Figs. 2, 4) and the SED (Fig. 6) simultaneously, we used a temperature-gradient model. This model consists of many thin rings emitting blackbody radiation at a local temperature $T(r) = T_0 \cdot (r/r_0)^{-q}$, where r_0 denotes the inner disk radius, T_0 the effective temperature at r_0, and q the power-law

Table 2. Observation log.

#	Night	Instrument	$B_{\rm proj}$ [m]	PA [°]	Seeing [″]	DIT [ms]	Calibrator	Calibrator diameter [mas]
I	2009-04-17	AMBER	15/30/45	259/259/259	0.55	200	HD 142669	0.256 ± 0.018^a
II	2009-05-22	AMBER	31/61/91	258/258/258	0.8	150	HD 142669	0.256 ± 0.018^a
III	2011-04-30	AMBER	59/68/71	238/126/176	1.0	300	HD 138472	1.07 ± 0.02^b
IV	2011-04-30	AMBER	63/70/72	256/141/193	0.8	300	HD 138472	1.07 ± 0.02^b
V	2004-06-07	MIDI	102	37	0.9	14	HD 146791	3.00 ± 0.033^c
VI	2004-06-07	MIDI	90	44	1.1	18	HD 169916	4.24 ± 0.047^c

Notes. $B_{\rm proj}$ denotes the lengths of the projected interferometer baselines during the observations, PA the baseline position angles, and DIT the detector integration time for recording individual interferograms. The resulting uv coverage is shown in Fig. 1.

References. [(a)] Lafrasse et al. (2010); [(b)] Richichi et al. (2005); [(c)] Bordé et al. (2002).

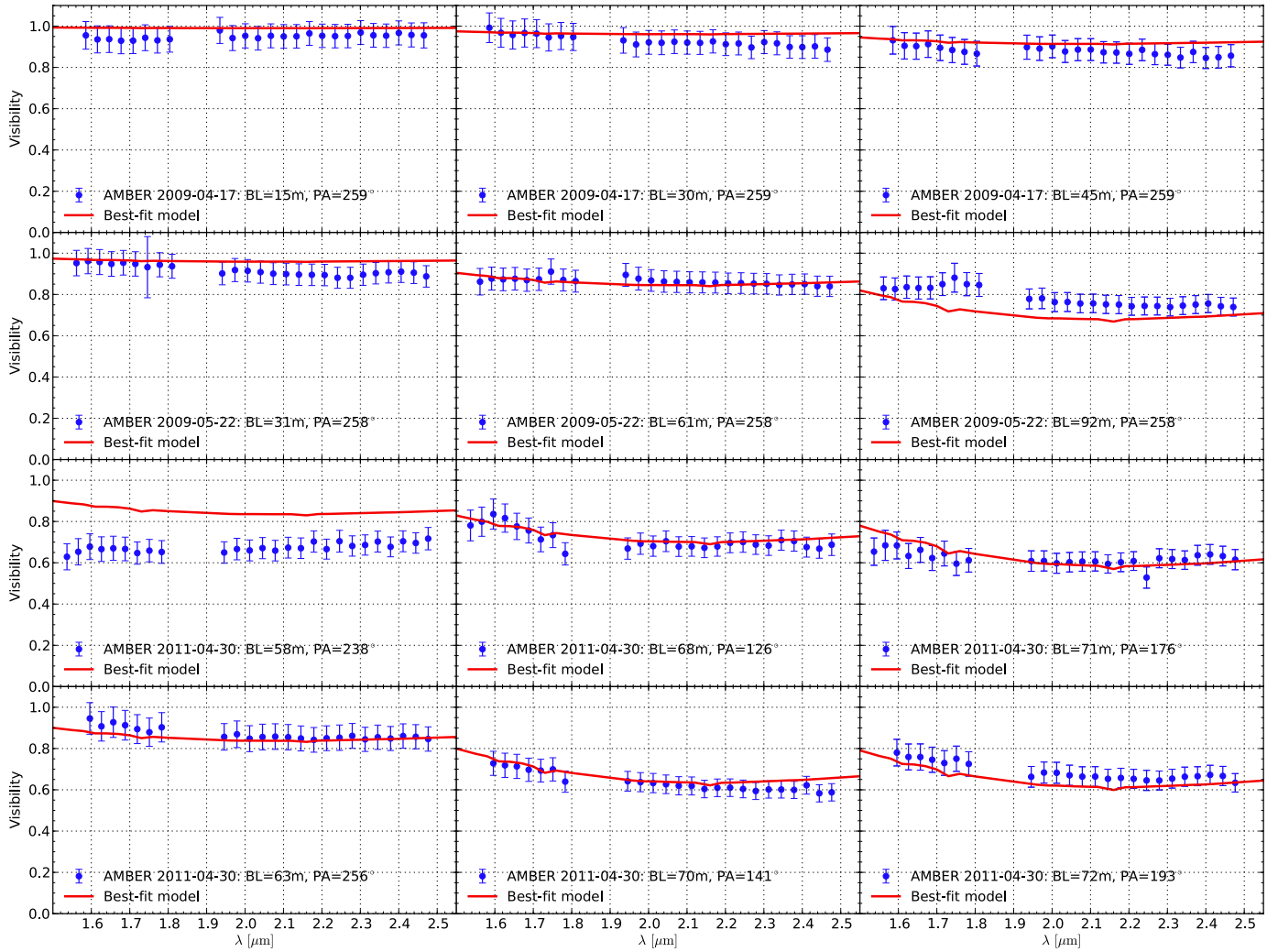

Fig. 2. AMBER visibilities (see Table 2) and temperature-gradient model B_3: the panels show the wavelength-dependent H and K band visibilities of our AMBER observations. Each panel displays one of the three baselines of each measurement (nights I-IV, cf. Table 2). The red line indicates the corresponding best-fit temperature-gradient model curves (model B_3 in Table 5) in all plots.

index. Other free parameters are the inclination i and the position angle ϑ of the semi-major axis of the disk. A more detailed description of our modeling of temperature-gradient disks can be found, for example, in Vural et al. (2012) or Kreplin et al. (2012).

We computed models for all mathematical combinations of the parameter values listed in Table 4. We chose the model with the lowest $\chi^2_{\rm red}$ value as the best-fit model. The given error bars are 3σ errors.

We first attempted to fit the data with a model consisting of a stellar point source (distance, L_*, and T_* from Table 1) and a temperature-gradient disk (model A in Table 4). The model has six free parameters: the inner ring radius $r_{\rm in,1}$, the width of the ring $\Delta r_{\rm in,1} = r_{\rm out,1} - r_{\rm in,1}$, the temperature at the inner radius $T_{\rm in,1}$,

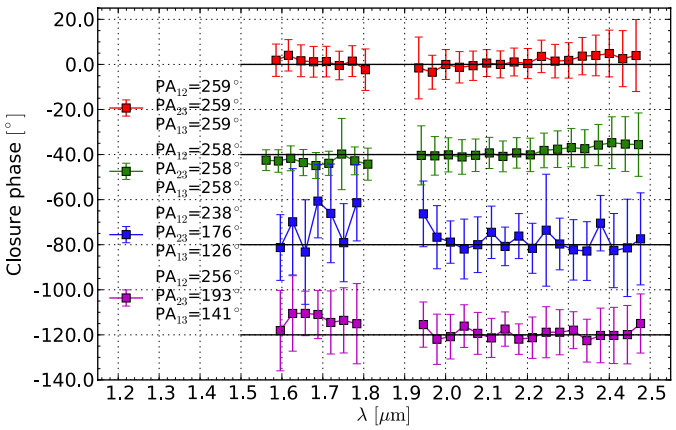

Fig. 3. Wavelength dependence of the closure phases of all AMBER measurements from Table 2. The curves are offset from each other by 40°. The respective zero line is indicated as a solid horizontal line.

the power-law index q_1, the inclination i, and the position angle of the semi-major axis of the disk-like object ϑ. The best-fit parameters are listed in Table 5. However, no successful fit could be found that is able to reproduce all observations simultaneously ($\chi^2_{\rm red} = 6.2$).

Therefore, we adopted a two-component model consisting of the star (same parameters as above) and two inclined concentric ring-shaped disks (model B, see Table 4 and 5). There are ten free model parameters: four for the inner disk ($r_{\rm in,1}$, $\Delta r_{\rm in,1}$, $T_{\rm in,1}$, q_1), four for the outer disk ($r_{\rm in,2}$, $\Delta r_{\rm in,2}$, $T_{\rm in,2}$, q_2), and two for the whole disk system (i, ϑ). We computed all combinations of these parameters within the parameter ranges (and for the described N step values) defined in Table 4. We first calculated the models with a rough grid (model B_1) and then with finer grids (model B_2 and B_3) around the $\chi^2_{\rm red}$-minimum of the previous run. In total (for all models described in Table 4), we computed ~700 million models.

In our best-fitting model B_3 ($\chi^2_{\rm red} = 2.7$, see Figs. 2, 4, and 6), the inner disk spans from 0.19 ± 0.01 AU to 0.23 ± 0.02 AU (with a temperature of 1257^{+133}_{-53} K at the inner radius $r_{\rm in,1}$) and the outer disk between $1.35^{+0.19}_{-0.20}$ AU and >4.3 AU (334^{+35}_{-17} K at $r_{\rm in,2}$) with a gap between both components. The very narrow disk width of 0.04 AU makes the inner disk region appear rather ring-like in the NIR (see Fig. 6, right). We cannot constrain the temperature gradient q_1 because the inner narrow ring-shaped component is basically emitting only at one uniform temperature $T_{\rm in,1}$. The inclination (angle between the system axis and the viewing direction) is $48.6^{+2.9\circ}_{-3.6}$ and the position angle of the disk is $169.3^{+4.2\circ}_{-6.7}$, which is approximately consistent with our geometric model in Sect. 3.1. We emphasize that the structure of the outer disk is a result of the longer wavelength data – that is, the MIDI data and the MIR/far-infrared (FIR) SED. The inclination and position angle of the system are mainly determined by the NIR interferometric data but consistent with the MIDI data. In the case of temperature-gradient models with more than one component, please note that simultaneous modeling of the visibilities and the SED is able to constrain the inner temperatures ($T_{\rm in,1}$, $T_{\rm in,2}$) of the single components rather than the exact shape of the single temperature gradients (q_1, q_2).

Table 3. Parameters of the best-fit geometric model.

Band	$r_{\rm ring,in}$ [AU]	i °	ϑ °	$f_{\rm star}$	$f_{\rm disk}$
H	0.15 ± 0.06	50 ± 11	179 ± 17	0.53 ± 0.10	0.47 ± 0.10
K	0.18 ± 0.06	49 ± 5	163 ± 9	0.33 ± 0.27	0.67 ± 0.27

Notes. The radius $r_{\rm ring,in}$ represents the inner semi-major axis of the inclined model ring; the position angle ϑ denotes the position angle of the semi-major axis; i is the inclination of the system axis to the line of sight, $f_{\rm star}$ the flux contribution from the star, and $f_{\rm disk}$ the flux contribution from the disk to the total flux (see text in Sect. 3.1). The errors of the radii include the distance error (116 ± 30 pc).

4. Discussion

To compare the disk size of V1026 Sco with other young stellar objects, we plot the K-band radius (0.18 ± 0.06 AU, see Table 3) obtained with a geometric inclined-ring fit into the size-luminosiy diagram (Fig. 7). The derived radius is ~1.5 times larger than expected for a dust sublimation temperature of 1500 K and is located approximately on the 1200 K line. Within the error bars, it still agrees with a dust sublimation temperature of 1500 K expected for dust consisting mostly of silicates (Natta et al. 2001; Dullemond et al. 2001; Monnier & Millan-Gabet 2002).

The derived best-fit temperature-gradient model B_3 consists of a two-component disk model; all parameters are listed in Table 5. The inner component is a ring-shaped disk with an inner radius of 0.19 ± 0.01 AU and an inner temperature of 1257^{+133}_{-53} K. The outer ring-shaped disk extends from $1.35^{+0.19}_{-0.20}$ AU to >4.3 AU with 334^{+35}_{-17} K at the inner edge. Between the hot inner and cool outer components, our best-fit model shows an approximately 1.1 AU-wide gap. The inclination of $48.6^{+2.9\circ}_{-3.6}$ is similar to the inclination derived with our geometric model in Sect. 3.1 (~49°and ~50°) and to the value of 55° found by Dominik et al. (2003). Neither of the power-law indices could be constrained. In the inner component, the ring width is too small to allow us to constrain q_1. In the outer component, there seems to be a degeneracy between q_2 and $r_{\rm out,2}$. The parameters of the inner disk (Table 5) are similar to the ones obtained with the geometric fit of the NIR visibilities (Table 3) and the size-luminosity diagram (Fig. 7). A possible explanation for the lack of FIR emission in the SED of some HAeBes and the apparent disk gap is self-shadowing by the puffed-up inner rim (Dullemond & Dominik 2004).

The stellar rotation of V1026 Sco is $v \sin i$ = 65.3 ± 3.1 km s^{-1} (Alecian et al. 2013a), leading to a maximum rotational velocity of ~86 km s^{-1} if the inclination of the star is comparable to the disk inclination. This is similar (Boehm & Catala 1995) or slightly lower (Alecian et al. 2013b) than the average velocity of low-mass Herbig Ae/Be stars but higher than measurements of T Tauri stars (Weise et al. 2010).

Magnetic braking can reduce the rotational velocity as observed in T Tauri stars (Koenigl 1991; Weise et al. 2010; Johnstone et al. 2014). In Herbig stars, strong magnetic braking is less likely than in T Tauri stars because the observed magnetic fields are weaker. In V1026 Sco, a magnetic field has not been detected (Alecian et al. 2013a), which could mean that it is weak, as expected for Herbig Ae stars (Weise et al. 2010). Even if a magnetic field exists, but could not be detected, the high value of the stellar rotation velocity of V1026 Sco suggests that rotational braking via disk locking (Koenigl 1991; Stępień 2000) is much weaker than in T Tauri stars.

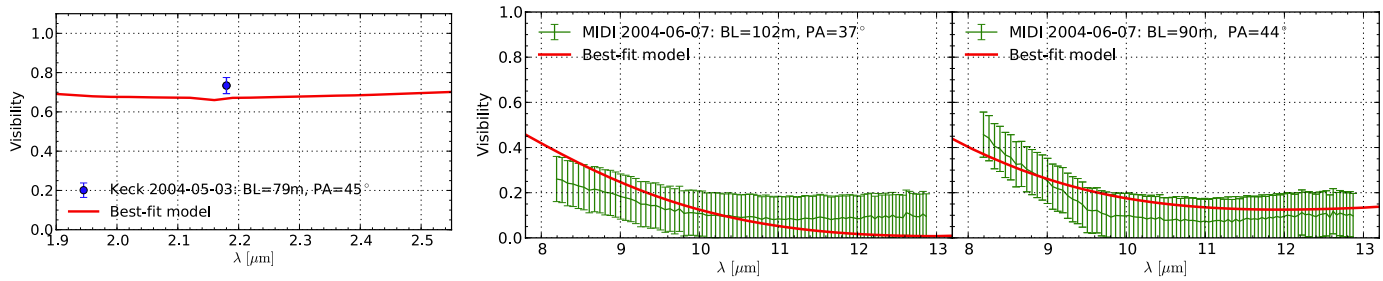

Fig. 4. Keck and MIDI observations and temperature-gradient model B_3. *Left*: Keck visibility. *Right*: MIDI visibilities.

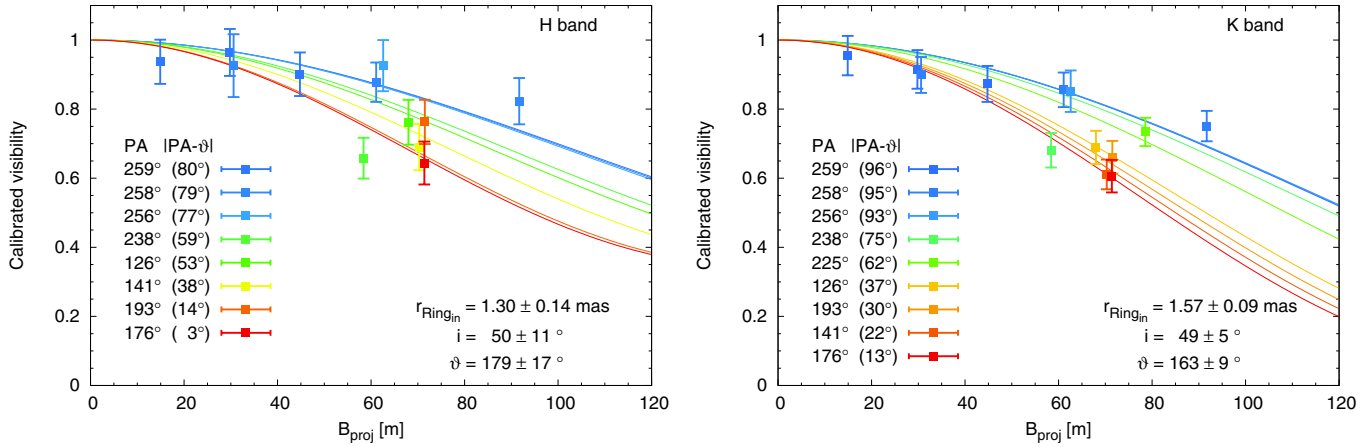

Fig. 5. Geometric inclined ring-fit models (ring width =20% of $r_{\mathrm{ring,in}}$) of the *H*- (*left*) and *K*-band (*right*) visibilities. The right plot contains our AMBER data and the KI measurements. The wavelengths are averaged over the whole respective spectral band. The model consists of the unresolved stellar contribution and an inclined ring (see Sect. 3.1). We simultaneously fit all visibilities with a two-dimensional visibility model. The model curves are plotted for all position angles for which visibilities were measured. The color sequence (blue to red) describes the decreasing difference between the PA of the measurement and the disk's fitted semi-major axis ϑ.

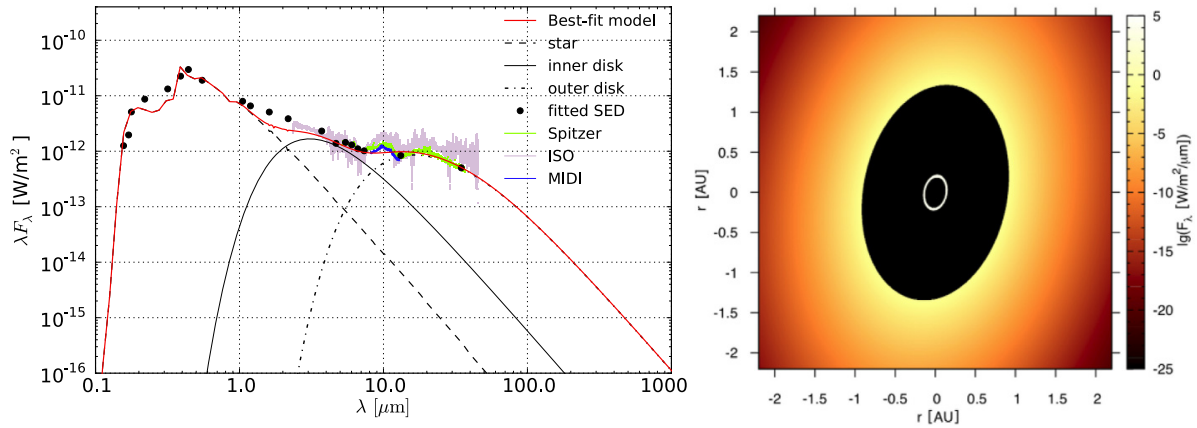

Fig. 6. *Left*: SED and temperature-gradient model B_3: the SED of V1026 Sco was constructed using published SED observations (black dots). Some of the points represent binned observations; the size of the error bars is on the order of the size of the dots. The resulting fit curve (red) consists of the stellar contribution (Kurucz model, black dashed line), the inner ring (black solid line), and the outer ring model SED (black dash-dotted line). *Right*: two-dimensional intensity distribution of our best-fit model (B_3) at 2 μm. The narrow bright ring is the inner ring-shaped disk in the model. The central star is not shown here. Please note that the intensity scale is logarithmic; the outer disk contributes only insignificantly to the NIR flux. The actual geometry of the outer disk remains poorly constrained because only two MIDI uv points exist.

Our findings can be described with the standard disk theories for Herbig Ae stars, which postulate passive circumstellar disks with inner holes and puffed-up inner rims (Natta et al. 2001; Dullemond et al. 2001). In addition, the derived inclination might be large enough to explain the UXOr variability of V1026 Sco in the context of current proposed theories, as we discuss in the following. Theories about partial obscuration of the stellar light by hydrodynamic fluctuations of the inner rim need high inclination angles for explaining the UXOr variability (Dullemond et al. 2003). With the measured intermediate inclination of V1026 Sco, the rim fluctuations would have to be twice as high as the theoretical fluctuation height. Therefore, this model is less suitable in our case and also for several other UXOrs (e.g. Pontoppidan et al. 2007). The unsteady accretion

Table 4. Scanned range of the parameters of the computed temperature-gradient models (A, B_1, B_2 and B_3).

Parameter	Range (A)	N(A)	Range (B_1)	N(B_1)	Range (B_2)	N(B_2)	Range (B_3)	N(B_3)
$r_{in,1}$ [AU]	0.01–1.0	30	0.05–1.0	8	0.1–0.3	8	0.15–0.25	10
$\Delta r_{in,1}$ [AU]	0.01–10	30	0.01–2.0	8	0.01–0.15	8	0.02–0.07	8
$r_{in,2}$ [AU]	...	...	0.05–3.0	8	0.4–2.0	8	1.0–1.7	8
$\Delta r_{in,2}$ [AU]	...	...	0.01–10	8	0.5–10	8	1.0–6.0	4
$T_{in,1}$ [K]	200–2000	30	800–2000	8	1000–1500	8	1200–1400	8
$T_{in,2}$ [K]	...	...	150–1000	8	100–400	8	300–380	8
q_1	0.2, 0.5, 0.75, 1.0	4	0.2, 0.5, 0.75, 1.0	4	0.2, 0.5, 0.75, 1.0	4	0.2, 0.5, 0.75, 1.0	4
q_2	...	...	0.2, 0.5, 0.75, 1.0	4	0.2, 0.5, 0.75, 1.0	4	0.2, 0.5, 0.75, 1.0	4
i [°]	0–90	30	0–80	6	10–60	6	40–60	8
ϑ [°]	0–170	30	0–160	6	130–180	6	150–180	8

Notes. The free model parameters for the inner ($j = 1$) and, if included, outer ($j = 2$) ring-shaped disk are as follows: the inner ring radius $r_{in,j}$, the ring width $\Delta r_{in,j}$, the temperature at the inner radius $T_{in,j}$, the power-law index q_j, the inclination i, and the position angle of the semi-major axis ϑ. The number of steps computed per parameter is given by N. The step spacing is logarithmic for $r_{in,1}$, $\Delta r_{in,1}$, and $r_{in,2}$, and is linear for the rest of the parameters except q_1 and q_2, for which the individual values used are given directly.

Table 5. Parameters of best-fit temperature-gradient models A and B_3.

Parameter	Best-fit parameters (A)	Best-fit parameters (B_3)
$r_{in,1}$ [AU]	0.06 ± 0.01	0.19 ± 0.01
$r_{out,1}$ [AU]	$4.6^{+1.1}_{-1.6}$	0.23 ± 0.02
$r_{in,2}$ [AU]	...	$1.35^{+0.19}_{-0.20}$
$r_{out,2}$ [AU]	...	>4.3
$T_{in,1}$ [K]	1937^{+25}_{-61}	1257^{+133}_{-53}
$T_{in,2}$ [K]	...	334^{+35}_{-17}
q_1	0.5	0.5
q_2	...	1.0
i [°]	$86.9^{+0.2}_{-1.7}$	$48.6^{+2.9}_{-3.6}$
ϑ [°]	$139.0^{+0.2}_{-1.7}$	$169.3^{+4.2}_{-6.7}$
χ^2_{red}	6.2	2.7

Notes. The listed parameters for the inner ($j = 1$) and, if included, outer ($j = 2$) ring-shaped disk are as follows: the inner ring radius $r_{in,j}$, the outer ring radius $r_{out,j} = r_{in,j} + \Delta r_{in,j}$, the temperature at the inner radius $T_{in,j}$, the power-law index q_j, the inclination i, and the position angle of the semi-major axis ϑ. Parameters without error bars cannot be constrained (see discussion in Sect. 4).

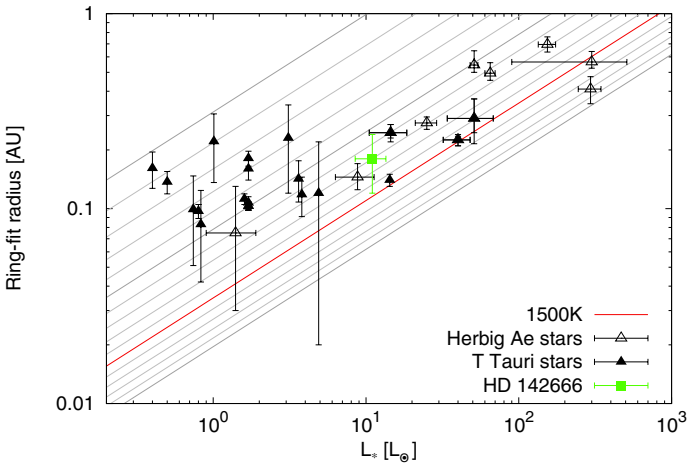

Fig. 7. Size-luminosity diagram. The K-band ring-fit radius of V1026 Sco (semi-major axis derived with an inclined ring fit in Sect. 3.1) is plotted as a green filled square. For comparison, we also plot a sample of Herbig Ae stars (unfilled black triangles, Monnier et al. 2005) and a sample of TTS (filled black triangles, Pinte et al. 2008). The theoretical relation between the ring radius in the NIR and the luminosity (Monnier & Millan-Gabet 2002) is shown for different temperatures. The 1500 K line is plotted in red; the gray lines indicate curves for temperatures between 500 K (highest line) and 2000 K (lowest line) in 100 K steps.

model by Herbst & Shevchenko (1999) is inclination independent and cannot be disproven with our measurements. For intermediate to high disk inclinations, orbiting dust clouds might intercept the line of sight toward the star (Grinin et al. 1994; Natta et al. 1997). For this case, the derived inclination of V1026 Sco is still within the range predicted for UXOrs (45°–68°) by Natta & Whitney (2000). Dust clouds in centrifugally-driven disk winds (Vinković & Jurkić 2007; Bans & Königl 2012) can also explain the UX Ori type variability of V1026 Sco, as they also are consistent with intermediate to high disk inclinations.

5. Conclusion

We observed the UX Ori star V1026 Sco with VLTI/AMBER in the H and K bands. With a geometric ring-shaped model consisting of the star and an inclined ring, we found a radius of $r_{ring,in} = 0.18 \pm 0.06$ AU in the K band. In the context of the size-luminosity diagram, this radius is found to be consistent with the theory of a passive circumstellar disk with an inner hole and a rim at the dust sublimation radius. We further derived an inclination of $50 \pm 11°$ and $49 \pm 5°$ and a PA of the semi-major axis of the inclined disk of $179 \pm 17°$ and $163 \pm 9°$ in the H and K bands, respectively.

We found a two-component-disk temperature-gradient model that is able to reproduce all visibilities and the SED. The inner radius of the inner disk is 0.19 ± 0.01 AU and similar to the one found with a geometric ring fit. The two disk components are separated by a gap, which may be explained by a shadow cast by a puffed-up inner rim and agrees with the type II classification of the object. The derived inclination of $48.6^{+2.9}_{-3.6}°$ and the PA of $169.3^{+4.2}_{-6.7}°$ are consistent with the values found by geometric modeling. Our inclination of ~49° is probably not consistent with a model where rim fluctuations cause the UXOr variability, because the expected rim height is not high enough, as discussed above. The unsteady accretion theory

cannot be excluded with our measurements, because the model is inclination-independent. Finally, the measured intermediate disk inclination is within the range predicted from UXOr models with orbiting dust clouds in the disk or in centrifugally-driven disk winds.

Acknowledgements. We would like to thank K. R. W. Tristram for helpful discussions and suggestions and also our colleagues at Paranal for their excellent collaboration. We thank the anonymous referees for the helpful comments.

References

Alecian, E., Wade, G. A., Catala, C., et al. 2013a, MNRAS, 429, 1001
Alecian, E., Wade, G. A., Catala, C., et al. 2013b, MNRAS, 429, 1027
Bans, A., & Königl, A. 2012, ApJ, 758, 100
Boehm, T., & Catala, C. 1995, A&A, 301, 155
Bordé, P., Coudé du Foresto, V., Chagnon, G., & Perrin, G. 2002, A&A, 393, 183
Chelli, A., Utrera, O. H., & Duvert, G. 2009, A&A, 502, 705
Dominik, C., Dullemond, C. P., Waters, L. B. F. M., & Walch, S. 2003, A&A, 398, 607
Dullemond, C. P., & Dominik, C. 2004, A&A, 417, 159
Dullemond, C. P., Dominik, C., & Natta, A. 2001, ApJ, 560, 957
Dullemond, C. P., van den Ancker, M. E., Acke, B., & van Boekel, R. 2003, ApJ, 594, L47
Folsom, C. P., Bagnulo, S., Wade, G. A., et al. 2012, MNRAS, 422, 2072
Grinin, V. P., The, P. S., de Winter, D., et al. 1994, A&A, 292, 165
Grinin, V. P., Kozlova, O. V., Natta, A., et al. 2001, A&A, 379, 482
Herbst, W., & Shevchenko, V. S. 1999, AJ, 118, 1043
Johnstone, C. P., Jardine, M., Gregory, S. G., Donati, J.-F., & Hussain, G. 2014, MNRAS, 437, 3202
Juhász, A., Bouwman, J., Henning, T., et al. 2010, ApJ, 721, 431
Kishimoto, M., Hönig, S. F., Antonucci, R., et al. 2011, A&A, 536, A78
Koenigl, A. 1991, ApJ, 370, L39
Kreplin, A., Kraus, S., Hofmann, K.-H., et al. 2012, A&A, 537, A103
Lafrasse, S., Mella, G., Bonneau, D., et al. 2010, VizieR Online Data Catalog: II/300
Lecavelier des Etangs, A., Nitschelm, C., Olsen, E. H., Vidal-Madjar, A., & Ferlet, R. 2005, A&A, 439, 571
Leinert, C., Graser, U., Przygodda, F., et al. 2003, Ap&SS, 286, 73
Meeus, G., Waelkens, C., & Malfait, K. 1998, A&A, 329, 131
Mendigutía, I., Calvet, N., Montesinos, B., et al. 2011, A&A, 535, A99
Monnier, J. D., & Millan-Gabet, R. 2002, ApJ, 579, 694
Monnier, J. D., Millan-Gabet, R., Billmeier, R., et al. 2005, ApJ, 624, 832
Natta, A., & Whitney, B. A. 2000, A&A, 364, 633
Natta, A., Grinin, V. P., Mannings, V., & Ungerechts, H. 1997, ApJ, 491, 885
Natta, A., Prusti, T., Neri, R., et al. 2001, A&A, 371, 186
Petrov, R. G., Malbet, F., Weigelt, G., et al. 2007, A&A, 464, 1
Pinte, C., Ménard, F., Berger, J. P., Benisty, M., & Malbet, F. 2008, ApJ, 673, L63
Pontoppidan, K. M., Dullemond, C. P., Blake, G. A., et al. 2007, ApJ, 656, 980
Richichi, A., Percheron, I., & Khristoforova, M. 2005, A&A, 431, 773
Schegerer, A. A., Ratzka, T., Schuller, P. A., et al. 2013, A&A, 555, A103
Stępień, K. 2000, A&A, 353, 227
Tatulli, E., Millour, F., Chelli, A., et al. 2007, A&A, 464, 29
van Boekel, R., Min, M., Waters, L. B. F. M., et al. 2005, A&A, 437, 189
Vinković, D., & Jurkić, T. 2007, ApJ, 658, 462
Vural, J., Kreplin, A., Kraus, S., et al. 2012, A&A, 543, A162
Weise, P., Launhardt, R., Setiawan, J., & Henning, T. 2010, A&A, 517, A88
Zwintz, K., Kallinger, T., Guenther, D. B., et al. 2009, A&A, 494, 1031